Quaternary Science Advances 5 (2022) 100046

Contents lists available at ScienceDirect

Quaternary Science Advances

journal homepage: www.sciencedirect.com/journal/quaternary-science-advances

Automated characterisation of glaciomarine sediments using X-ray computed laminography

Neil McDonald [a,*], Tom Bradwell [a], S. Louise Callard [b], Jaime L. Toney [c], Briony Shreeve [d], James Shreeve [d]

[a] Biological and Environmental Sciences, University of Stirling, Stirling, FK9 4LA, UK
[b] School of Geography, Politics and Sociology, Newcastle University, Newcastle upon Tyne, NE1 7RU, UK
[c] School of Geographical & Earth Sciences, University of Glasgow, Glasgow, G12 8QQ, UK
[d] Geotek Ltd, 4 Sopwith Way, Daventry, Northamptonshire, NN11 8PB, UK

ARTICLE INFO

Keywords:
X-radiography
Laminography
Glaciomarine
Sediments
Ice-rafted debris

ABSTRACT

This study investigates the potential of a new high-resolution, non-destructive, X-ray imaging technique for the Quaternary Sciences – computed laminography (CL). Greyscale properties are systematically extracted from digital X-radiographic CL images of cored glaciomarine sediments to analyse and characterise sediments at pixel-scale resolution (<0.1 mm). We show how this can be achieved manually, and also with an easy-to-use, automated statistical tool which we have devised specifically for use in glaciomarine sediments. This Sediment Characteristics tool, in the form of a plugin for the freely available FIJI/ImageJ programme, extracts mean or median X-ray grey values (GV) – a proxy for sediment density; and associated standard deviation (SD) – a proxy for sediment heterogeneity – at sub-mm resolution, across the width of sediment core CL images. We demonstrate how these properties (GV and SD) can be directly used to characterise sediment properties and in particular to quantify the abundance of gravel clasts, or ice-rafted debris, in cored glaciomarine sediments. The tool's effectiveness is compared with other, more traditional, X-radiographic methods for counting ice-rafted gravel clasts in glaciomarine sediment. We propose that the CL output and Sediment Characteristics tool also have the potential to quantitatively analyse other 3-dimensional structures, such as cyclic lamination (varve) geometry; deformation structures; bioturbation and void space (porosity). Finally, we present the raw code, allowing open-access, transparency and reproducibility in other formats.

1. Introduction

The reconstruction of glaciers and ice sheets is vitally important for understanding past and projecting future environmental change (e.g. Clark et al., 2012; Gowan et al., 2021). In order to better constrain models of ice-sheet response to climate change, robust reconstructions of past ice sheets are essential. In marine settings, this is of particular importance due to instabilities inherent to marine ice sheets and tidewater glaciers (Scambos et al., 2004; Rignot et al., 2004; Schoof, 2007; Favier et al., 2014).

One way to track ice sheet and tidewater glacier instability is through terrigenous sediments that are transported to the ocean predominantly via iceberg rafting or meltwater pulses and leave distinct sedimentary signatures on the seafloor (Syvitski et al., 1996). Ice-rafted debris (IRD) forms a key component of glaciomarine reconstructions and represents a powerful proxy for past iceberg presence. IRD is chiefly used to infer past iceberg flux, however, concentrations of IRD may be biased by contrasting sediment inheritance due to the presence/removal of ice shelves (Reilly et al., 2019; O'Regan et al., 2021), ocean temperature changes or iceberg melt rates (Andrews, 2000), and changes in ocean currents (Starr et al., 2021). The identification and quantification of IRD allows reconstructions of global climatic events (Heinrich, 1988; Bond and Lotti, 1995; Obrochta et al., 2014; Margari et al., 2020); the growth, demise and deglaciation of ice sheets (Scourse et al., 2009; Hibbert et al.,

Abbreviations: Computed laminography, (CL); Computed tomography, (CT); X-radiography, (XR); Grey value, (GV); Standard deviation, (SD); Ice-rafted debris, (IRD).

* Corresponding author.
E-mail addresses: neil.mcdonald@stir.ac.uk (N. McDonald), tom.bradwell@stir.ac.uk (T. Bradwell), louise.callard@newcastle.ac.uk (S.L. Callard), Jaime.Toney@glasgow.ac.uk (J.L. Toney), briony@geotek.co.uk (B. Shreeve), james@geotek.co.uk (J. Shreeve).

https://doi.org/10.1016/j.qsa.2021.100046
Received 9 August 2021; Received in revised form 20 November 2021; Accepted 29 November 2021
Available online 2 December 2021

2010; Pierce et al., 2017); as well as high resolution ice stream and ice shelf processes – including calving intensities (Andresen et al., 2011) and collapse events (Kilfeather et al., 2011; Vermassen et al., 2020). Despite ice-rafted sediments providing a valuable record of past environmental change, the best way to characterise IRD in sediments remains contentious and non-standardised.

Particle-size discrimination is generally used to distinguish IRD, with icebergs transporting larger-grade sediments – usually in the sand (>0.63 μm) or gravel (>2 mm) fractions (cf. Andrews, 2000; Grobe, 1987; Scourse et al., 2009) – over greater distances than suspended sediments – usually fine silt or clay (<0.16 μm). IRD layers may also be characterised by greater heterogeneity (i.e. be more poorly sorted) than sediments formed through 'normal' glaciomarine sedimentation from settling via meltwater discharge from marine-terminating glaciers (Dowdeswell et al., 2000, 2001).

Currently, there are two main approaches for characterising IRD, these use: (1) grain abundances or (2) sediment fractions by volume or weight. These different approaches can use destructive methods, typically for fine-grained material (sensu Scourse et al., 2009; Vermassen et al., 2019) or non-destructive X-ray-imaging methods on coarser clastic material (>~1 mm or >2 mm) (sensu Grobe, 1987; Bartels et al., 2017). The most commonly employed technique remains a grain-counting method introduced by Grobe (1987), which employs manual counts of the number of clasts >2 mm for every 1 cm slice of sediment in traditional 2-dimensional X-radiographs (XR) to represent the ice-rafted fraction of sediments. Owing to its relative ease, familiarity, and non-destructive nature, this method remains popular today, more than 30 years after its introduction (e.g. Graham et al., 2017; Jennings et al., 2018; Joe et al., 2020).

The application of X-ray computed tomography (CT) in Quaternary science has advanced significantly in recent years. X-ray attenuation coefficients (grey values, CT numbers or Hounsfield units), a proxy for density (Reilly et al., 2017; Tonai et al., 2019), have been used to identify sedimentary structures in different depositional settings, including glacial and postglacial environments (St-Onge and Long, 2009; Jennings et al., 2018); as well as bottom-current velocity variations (Vandorpe et al., 2019); and precise varve counting (Damci and Çağatay, 2015). Additionally, X-ray attenuation coefficients have been used to effectively discriminate sediment facies based on differences in radiodensities (in Hounsfield units) between sedimentary structures (Mena et al., 2015), suggesting that the radiodensity of sediments can provide diagnostic criteria on the nature of sedimentation, facies depositional setting and genesis. Innovations in quantitative analyses using CT scans of sediment cores have introduced a new framework for the analysis of glaciomarine sediments typically through the MATLAB™ interface SedCT (Reilly et al., 2017). Radiodensity thresholding allows a quantification of the percentage coverage or number of all clasts (>1 mm) per unit area (Bartels et al., 2017; Reilly et al., 2019). Additionally, the standard deviation (SD) of the remaining fine grained (<1 mm) fraction may be assessed using the horizontal SD of radiodensities (in Hounsfield units) across the width of the image (Bartels et al., 2017). This type of analysis is not yet widely reported, however, it suggests that radiodensity SD can be used to assess fine:coarse-grained compositional ratios and infer former depositional styles in certain settings.

Two X-ray imaging approaches currently dominate the analysis of cored sediments: 2-dimensional XR and 3-dimensional CT. XR is by far the most common method for cost and practicality reasons, and is routinely applied in glaciomarine sediment analyses (e.g., Graham et al., 2017; Joe et al., 2020; Bradwell et al., 2021). XR produces an averaged 2D projection of the whole or split sediment core, whereby the X-ray beam passes through the core and an image montage is produced as the core moves past the X-ray source and detector. CT is a higher cost, data intensive, longer exposure-time technique, which has gained popularity in the geosciences over the last two decades. The CT method involves acquiring X-ray projections from 360° around the core (or less for limited angle CT); these data 'slices' are then processed to create axial views or true 3D data representations (e.g., Bartels et al., 2017; Hodell et al., 2017). Whole core CT scans are performed on large medical-grade scanners, however availability is growing outside of hospitals. A third type of X-ray scanning technique, computed laminography (CL), produces thin 2D scans of an object at specified depth intervals. Through computed reconstruction of these 2D scans, the interior of the object can be imaged in sharp focus without the depth-averaging of traditional projection XR scans. As a valuable non-destructive technique, CL is increasing in prominence in the geosciences (e.g. Zuber et al., 2017) but has not yet been used to investigate glaciomarine sediments.

This article proposes a new non-destructive, automated, high-resolution method for discriminating IRD in cored glaciomarine sediments based on a combination of practical application and theory. The study tests whether automated sediment classifications can be effectively derived from X-ray CL properties of cored sediments using freely available image processing and statistical software (FIJI/ImageJ) (Schindelin et al., 2012). Wider applications, strengths and methodological uncertainties are also discussed.

2. Methods

Glaciomarine sediments were recovered by piston core from the present-day seafloor off NW Scotland (See Bradwell et al., 2021 for details of core recovery, locations, descriptions, etc.). Four split half-round sediment cores are presented, which were scanned using a Geotek XCT X-ray core scanner. All four split cores were scanned once using traditional projection XR, and scanned a second time using the CL technique. Digital images are presented in radiodensity positive form of separate scans using CT and CL [0.066 mm x-y plane resolution]. Of the core sections, three predominantly comprise mud-silt laminae of varying clastic content ranging from gravel-rich to gravel-free (JC123-032PC-section-05, JC123-032PC-section-06, JC123-033PC-section-06); the fourth core section contains a matrix-supported, generally structureless, glaciomarine diamicton (JC-123-033PC-section-05). A comprehensive list of operations and scripts implemented within this study are provided (see Supplementary Information).

2.1. Image acquisition: X-ray computed laminography

This study utilises the popular XR scanning technique by way of comparison with the new CL scanning method for sediment core analysis. CL produces 'thin slice' cross-sectional internal images of samples, typically through an angular intrusion of the X-ray beam (see Gondrom et al., 1999; Xu et al., 2012). In this study CL is implemented using an adaptation of XR by translational laminography, whereby the need to rotate samples is negated, hence this method is well suited to sediment core scanning (Fig. 1). CL exhibits less excessive X-ray attenuation than traditional XR scanning methods, reducing cupping artifacts and producing higher image quality (in the plane parallel to the object face)

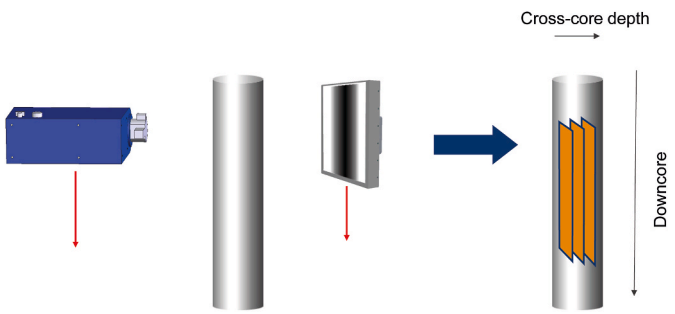

Fig. 1. Translational computed laminography method. X-rays are omitted from the source and pass through the sediment core before they are captured by a detector, where an algorithm is used to reconstruct images at 'thin sections' at specified depth intervals of the core.

with higher contrast of 'flat' samples. This results in increased fine-detail resolution compared to CT approaches (Xu et al., 2012; Zuber et al., 2017; Fisher et al., 2019). However, to our knowledge, it has not yet been documented whether CL images are of improved contrast and clarity with reduced artifacts when scanning glaciomarine sediments. This is also investigated in our study.

2.2. Image pre-processing

Initially, a beam-hardening correction algorithm was applied to reduce cupping due to greater X-ray attenuation within the thicker region at the centre of cores. This correction was manually applied using the Geotek Gquickview software. Images were then imported to FIJI/ImageJ to evaluate the degree of cupping due to beam hardening using a quadratic curvature coefficient (Fig. 2). The rectangular selection tool was used to select the grey values over the whole core width (horizontally). These data were then exported to Microsoft Excel (which was selected for this specific analysis due to flexibility with data manipulation) where the degree of cupping was investigated and detrended using a quadratic polynomial function ($y = ax^2 + bx + c$). This was repeated for XR and CL scans pre- and post-beam hardening and the curvature coefficient ('a' within the polynomial function) was used to highlight the degree of cupping. The greater the 'a' value, the greater the degree of cupping; slight overcorrections, are represented by negative values.

These data were then used to determine the optimal sampling window, as displayed in Fig. 2. The optimal sampling window is one where the curvature coefficient (a) of grey values across the width of the image is as close to 0 as possible. A manual, iterative approach is used where the beam hardening algorithm is altered and tested several times until the lowest possible degree of cupping, without overcorrection, is attained. Edge effects, including any laminae bending during piston core recovery (Skinner and McCave, 2003), may be avoided by selecting a further reduced-width window free from distorted or blurred edges at the image margins (Fig. 2, yellow boxes). An additional step was required if laminae exhibit a significant slope or inclination. This involved measuring the inclination in FIJI using the straight-line tool across laminae. The image was then rotated by the laminae inclination angle. Finally, images were then cropped to the sampling window size allowing analysis of the sampling window only.

2.3. Sediment characterisation tool

The Sediment Characteristics (SC) plugin utilises the straight line-profile tool in FIJI/ImageJ to produce a horizontal line across the sampling window width (code provided in Supplementary Information). The mean grey value (GV) and grey value SD across this horizontal line are measured at pixel intervals downcore i.e., if an image is x pixels in length, the SC plugin will sample x measurements. The mean or median GVs provide a very high-resolution proxy for sediment density and the associated SD a proxy for sediment heterogeneity (or degree of sorting) (Fig. 3). Two videos illustrating the process are presented (see Supplementary Information).

Supplementary videos related to this article can be found at https://doi.org/10.1016/j.qsa.2021.100046

2.4. Characterising sediments by X-ray imaging properties

Initially, the SC tool was used on all four split-cores to highlight the applicability of the method for conveniently and non-destructively identifying the type and nature of sediments at very high-resolution (<0.1 mm). When comparing the pixel-interval sampled GV SD result to existing IRD methods, the sum of standard deviation per cm was totalled to allow a like-for-like direct statistical comparison to other more common practices (see below). Secondly, images were sampled incrementally at 10-pixel intervals and plotted on a scatter plot (mean GV vs SD) to identify any trends in imaging properties. Measurements from the first and last ~700 pixels on each image (~5 cm on 1-m-long cores) were removed as outliers, due to overestimations from a scanning artifact which occurs as a result of X-ray scatter around the ends of the core samples. Finally, three facies were then discriminated quantitatively based on clast abundances using the Folk sediment classification scheme whereby glaciomarine sediments are grouped based on gravel content (>2 mm) (adapted from Long, 2006). These facies classes were *clast-free* (<1% gravel), *clast-poor* (1–5% gravel) and *clast-rich* (5–30+% gravel). 50 random samples of each facies were interrogated via their X-ray CL imaging properties (mean GV and SD). These 50 measurements included both dense laminae and less dense laminae. Clasts (>2 mm) diameter were selected from existing clast maps (see below) (clasts >0.5 mm diameter) using the 'Analyze Particles...' function, by selecting particles with an area >3.14 mm^2 – the minimum area for clasts >2 mm in diameter (modified from Reilly et al., 2019). The clast abundance (%)

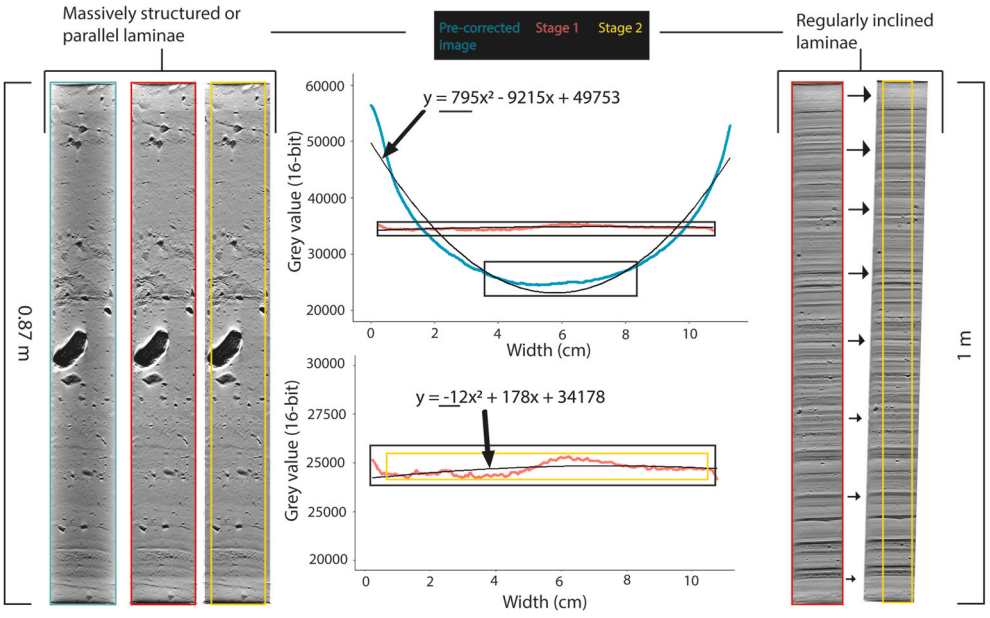

Fig. 2. Two-stage sampling window selection method which differs slightly for sediments with inclined laminae (annotated on right). Stage 1 involves beam hardening correction as illustrated from changes between blue to red (boxes and lines). Note: some data naturally cropped on core edges during beam hardening correction. Stage 2 involves cropping images free from blurred or disturbed cores edges (yellow boxes). For inclined laminae, stage 2 also involves rotating images at the inclination of laminae until horizontally parallel. Line plots indicate degree of cupping due to beam hardening. Illustrated by polynomial functions (curvature coefficients underlined) pre-beam hardening correction a = 795, post-beam hardening correction a = −12 (apparent 'overcorrection' due to greyscale variation in sediments). Black/yellow boxes: sampling windows. Note: greater sampling window for images post-beam hardening corrections. (For interpretation of the references to colour in this figure legend, the reader is referred to the Web version of this article.)

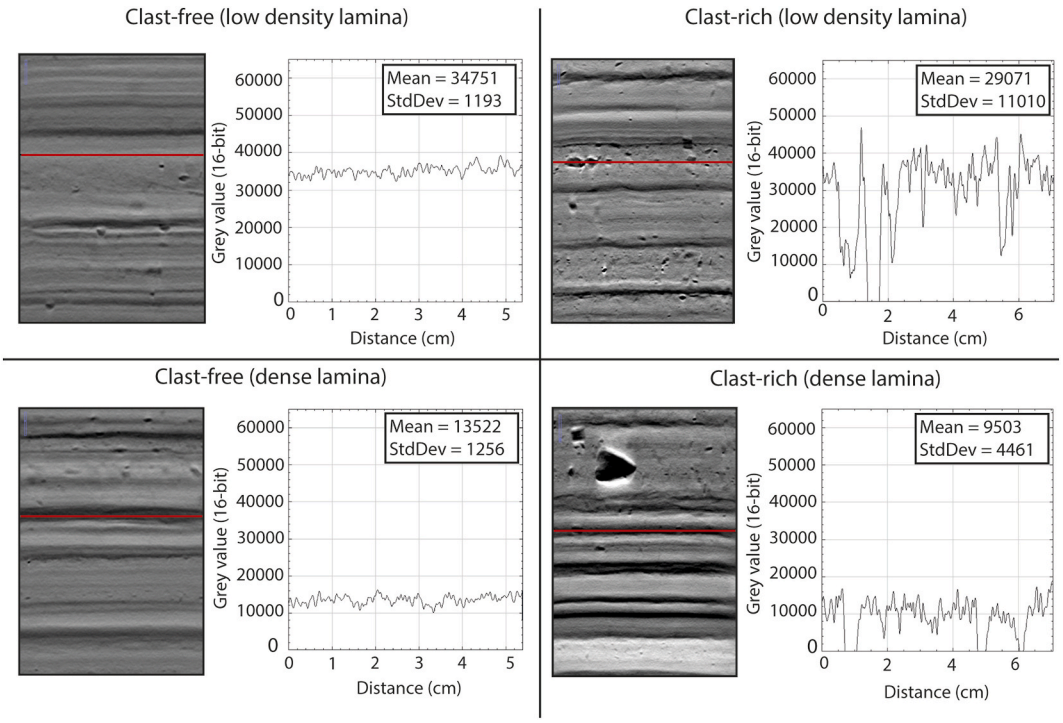

Fig. 3. Sediment classification based on X-ray imaging properties (grey value mean and standard deviations). In these (positive) X-radiographic images, lower density sediment is reflected as higher grey values (= whiter); high density sediment as lower grey values (= darker). Each negative departure from the mean represents a high-density (low grey value) clast or grain; positive departures may represent low-density sediment, voids or edge-effect 'halos' associated with clasts.

from clast maps extracted using the 'Area Fraction' function (at pixel resolution across core for each measurement) was directly compared to the corresponding greyscale image properties (mean GV and GV SD). Scatter plots were used to visually discriminate the characteristics and tendencies of these statistically classified sediments.

2.5. Comparison with existing IRD-identification methods

Alternative IRD detection methods use medical-grade CT scanning (Bartels et al., 2017; Reilly et al., 2019). To test one of these detection methods we isolated clasts (>~0.5 mm) on CL images and derived the % of clasts per unit area of sediment. After trialling an automated segmentation method (adapted from Principato, 2005) using the FIJI/imageJ threshold function, manual segmentation was preferred. This was due to flocculated silt or fine sand layers falling within the radiodensity threshold, as originally outlined by Reilly et al. (2019). Three of the cores in this study have dense laminae which resulted in overestimations in volume fraction methods, contrary to the results of the massive (non-laminated) core section (JC123-033PC-section-05) which showed a degree of correlation with manual segmentation methods (Fig. S1). Segmentation was applied for each core by isolating clasts manually by outlining; images were subsequently converted into binary (8-bit) images using density thresholding. The % volumes of identifiable clasts were then calculated for the width of the sampling area, in 1 cm intervals downcore (Supplementary Information).

On-screen grain counting (sensu Grobe, 1987) at 1 cm depth intervals, was also undertaken on all four cores. Gravel clasts (>2 mm), considered to be ice-rafted debris, were summed over 1 cm downcore increments. Both these methods (i) volume % of clasts using binary image 'thresholding' (sensu Bartels et al., 2017) and (ii) grain counting (sensu Grobe, 1987) are compared statistically with the sediment heterogeneity output (GV SD) from the Sediment Characteristics (SC) tool using Pearson's correlation coefficient.

3. Results

When comparing sediment heterogeneity (GV SD) data with other IRD measurement techniques or proxies in the same cores, generally good agreement is observed. Each of the methods (sediment heterogeneity, grain counting and volume fractions) are broadly synchronous in their peak distributions of IRD characterisation. However, the magnitude of peaks differs between methods (Fig. 4).

There are strong, statistically significant, correlations when comparing automatically generated sediment heterogeneity (using GV SD) with the observed proportion of clastic grains (% volume >~0.5 mm) in each core section ($r = 0.72–0.87$; $p = <0.001$) (Fig. 5). The highest correlation was seen in massive matrix-supported diamicton (JC123-033PC-05; $r = 0.87$); and the lowest on clast-poor strongly laminated mud (JC123-033PC-06; $r = 0.72$). The statistical correlations when comparing GV SD to clast counts are less strong ($r = 0.32–0.69$). Although all four core sections show statistically significant relationships ($p < 0.001$), the correlation coefficients (r) from the clast count data are lower than the area % clast data (Fig. S2; Table 1).

Distinct sedimentary structures are observed in the very high-resolution (<0.1 mm) CL images. Most apparent is the evidence of prolonged relatively high GV SD, indicative of clast-rich layers. Conversely, structureless and clast-free muds are characterised by a low GV SD signal (Fig. 6). The radiodensity (=GV) of sediments, a function of density and/or atomic number, can be affected by either sediment matrix (Fig. 6a) or clast proportion and clast density (Fig. 6b). However, it appears that the largest control on sediment density in these cores is from fine-sediment variations (most evident in Fig. 6a). The effect of fine sediment (matrix densities) as the largest control on sediment radiodensity, however, breaks down when gravel percentages are very high (>~30%), where large abundances of dense clasts raise the average density of sediment, despite low radiodensity matrices (Fig. 6b).

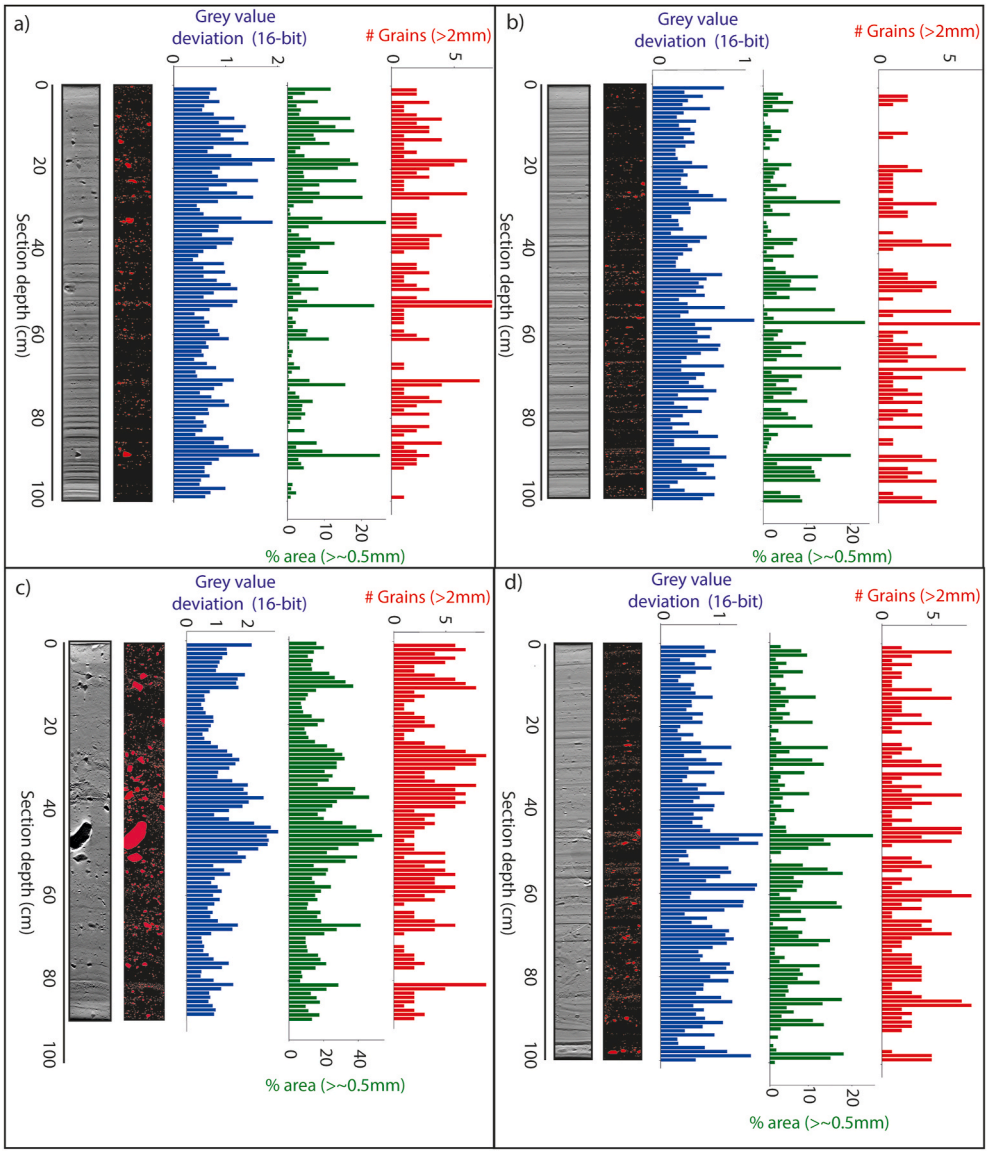

Fig. 4. Comparison of different IRD proxy measurement techniques. Blue bars: sediment heterogeneity (grey value standard deviation; summed area under curve per cm); green bars: % area of clasts (>~0.5 mm) per cm; red bars: traditional grain counts (>2 mm) at 1 cm downcore intervals. a) JC123-032PC-section-05; b) JC123-032PC-section-06; c) JC123-033PC-section-05; d) JC123-033PC-section-06. Note summed standard deviation (blue bars) expressed in standard form (1×10^6). (For interpretation of the references to colour in this figure legend, the reader is referred to the Web version of this article.)

3.1. Glaciomarine sediment characterisation

Extracting sediment mean GV and sediment heterogeneity values (GV SD) at regular 10-pixel intervals generates a data-point cloud between ~23000 and 38000 (mean GV) and ~1000–5000 (SD). There is no discrete clustering of different sediment facies by X-ray characteristics, with sediment characterisation appearing gradational across different classes (Fig. 7a). However, when attributing sediment heterogeneity (GV SD) to the corresponding Folk classification by gravel abundance (% clasts >2 mm), clear classification groups appear (Fig. 7b). This confirms that cored sediments can be effectively classified by their greyscale image properties (GV mean and GV SD) into well-established Folk sediment classification categories. The statistically significant relationship between % clast abundance (>~0.5 mm) per cm and the sum of GV SD (per cm) is validated by a similarly strong relationship between % clast abundance of gravels (>2 mm diameter) and GV SD both sampled at pixel-scale resolution ($p < 0.001$, $r = 0.808$) (Fig. 8).

4. Discussion

4.1. X-ray computed laminography: comparisons with conventional X-ray imaging techniques

CL represents a currently under-utilised approach in Quaternary science highly tailored towards extracting X-ray attenuation coefficients and deriving valuable non-destructive information on sediment properties. The resolution of CL images is significantly greater (ca. 5–7 times) than existing methods using medical-grade CT and allows analysis of mm-sized clasts and finer details (0.066 mm in this study vs 0.35–0.5 mm; cf Bartels et al., 2017; Reilly et al., 2019). Due to the 'thin slice' approach, CL images can be less data intensive than CT scanning approaches, this can reduce scanning times and data processing.

It should be noted, however, that CT has significant merits. Researchers are currently offered a trade-off between the different cost vs analytical capabilities of CT, CL or XR. Bespoke 3D CT scanners now exist which have been designed to generate higher-resolution images for geological applications (e.g. Condron and Hill, 2021). The 3D nature of CT allows for analysis of sedimentary structures in full 3D space, including 3D clast maps (see Bartels et al., 2018) which may allow analysis of clast properties (e.g., size and angularity) more robustly than

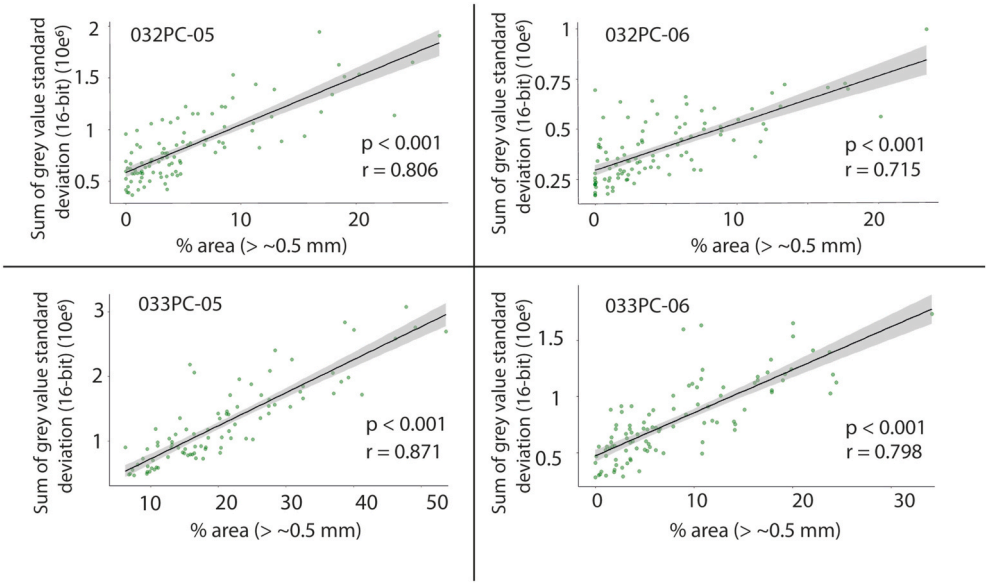

Fig. 5. Scatter plots of X-ray grey value, expressed as sum of standard deviation (i.e. sediment heterogeneity), per 1 cm downcore area vs % of clasts per 1 cm area; with associated Pearson's correlation coefficients shown (r).

Table 1
Pearson's correlation coefficients (r) between the sum of sediment heterogeneity (grey value standard deviation) per cm; number of clasts per cm downcore; and % area of clasts per cm for each core section.

Core section	# of clasts > 2 mm (r)	% area of clasts (r)
JC123-032PC-section-5	0.540	0.806
JC123-032PC-section-6	0.692	0.715
JC123-033PC-section-5	0.440	0.871
JC123-033PC-section-6	0.322	0.798

2.5D CL and 2D XR images. Using CT image processing software such as SedCT or Amira (Reilly et al., 2017; Bartels et al., 2017), grey values can be analysed from CT images without any bias from voids, cracks or scanning artifacts (Reilly et al., 2017) and in some cases without the bias of larger clasts (Bartels et al., 2017) by removing them after segmentation. In this area, CT images could prove more powerful than our CL sediment characterisation method. To account for this, we also include use of the median GV in the script, as in some cases this may prevent sediment density overestimation from anomalous dense clasts. CT scans also use CT numbers, which translate easily to absolute density (in Hounsfield units) (Reilly et al., 2017). By comparison, XR and CL images measure X-ray attenuation on a relative GV scale – although methods for calibration do exist (Francus et al., 2015). Calibration will always be preferable for studies comparing imagery between a large number of different cores.

Although XR may produce images at the same resolution, CL produces higher quality, sharper, more detailed images in the x-y plane (Fig. 9d). CL is stated to be more suited than XR and CT to laterally extended samples due to reduced variations in beam transmission during scanning (Helfen et al., 2007). This effect is also observed in this study when sampling split glaciomarine sediment cores. With 2D XR excessive X-ray attenuation towards the centre of circular cores where sediment is thicker results in a high degree of cupping (Fig. 9 panels a–c) and striping artifacts (Fig. 9d). The lower degree of beam hardening in CL images allows quantitative GV extraction at depth-specific intervals, while maintaining large sampling windows. In XR images, with a higher degree of beam hardening, the sampling window is significantly reduced (Fig. 2). Our findings show that CL is better suited to quantitatively analysing X-ray attenuation coefficients (or sediment radiodensities) on split cores, not only due to improved image quality, but also artifact reduction, with images exhibiting a consistent generally 'flatter' appearance (Fig. 2; Fig. 9). Thus, although the SC analysis could be performed on XR images, the reduced image quality and artifacts with XR (e.g. striping, cupping and surface effects) renders these images significantly less well suited to this style of quantitative image analysis. The relative benefits and disadvantages of X-ray CL are examined further (below) in relation to IRD analyses.

4.2. The benefits of using sediment heterogeneity to detect and characterise IRD

Sediment heterogeneity (GV SD) provides a highly reliable IRD proxy merited by its efficiency and lack of observer bias. Using the 'Sediment Characteristics' FIJI/ImageJ plugin presented here can reduce IRD estimation times significantly when compared to on-screen manual grain counting. Moreover, by employing X-ray CL, clast abundance can be quantified at significantly higher resolution. The greatest difference between GV SD and existing IRD methods is observed when compared to manual grain counting (Fig. S2). This is likely because the three IRD measurements quantify IRD in very different ways: (1) sediment heterogeneity (GV SD) is a function of the spread of relative sediment density values; (2) on-screen grain counts are a function of the absolute (or total) number of grains (>2 mm); and (3) volume fractions are a function of the size of grains (>~0.5 mm) per sampling region. Sediment radiodensity variations are observed to be more closely associated with the percentage area coverage of clasts on images, rather than clast abundance (grain counts). This is most evident in core section JC123-033PC-section-05 (Fig. 4c) where at ca. 42–55 cm large and very dense clasts covering most of the image are significantly underestimated by the grain counting method (and see Fig. S2), However, towards the base of the core (~79 cm) where there are a number of small, relatively low-density clasts, % area of clast and GV SD methods both underestimate the proportion of these smaller clasts. Therefore, we propose that combining sediment heterogeneity (GV SD) and grain counting may allow for a more efficient multiproxy approach, capable of better quantifying the contribution of iceberg-rafted debris to glaciomarine sediments.

The strong statistically significant relationship between gravel abundance (%) and GV SD allows classification of sediments using the modified Folk classification scheme (Long, 2006) and also provides appropriate calibration (Fig. 7b). This result is consistent with our

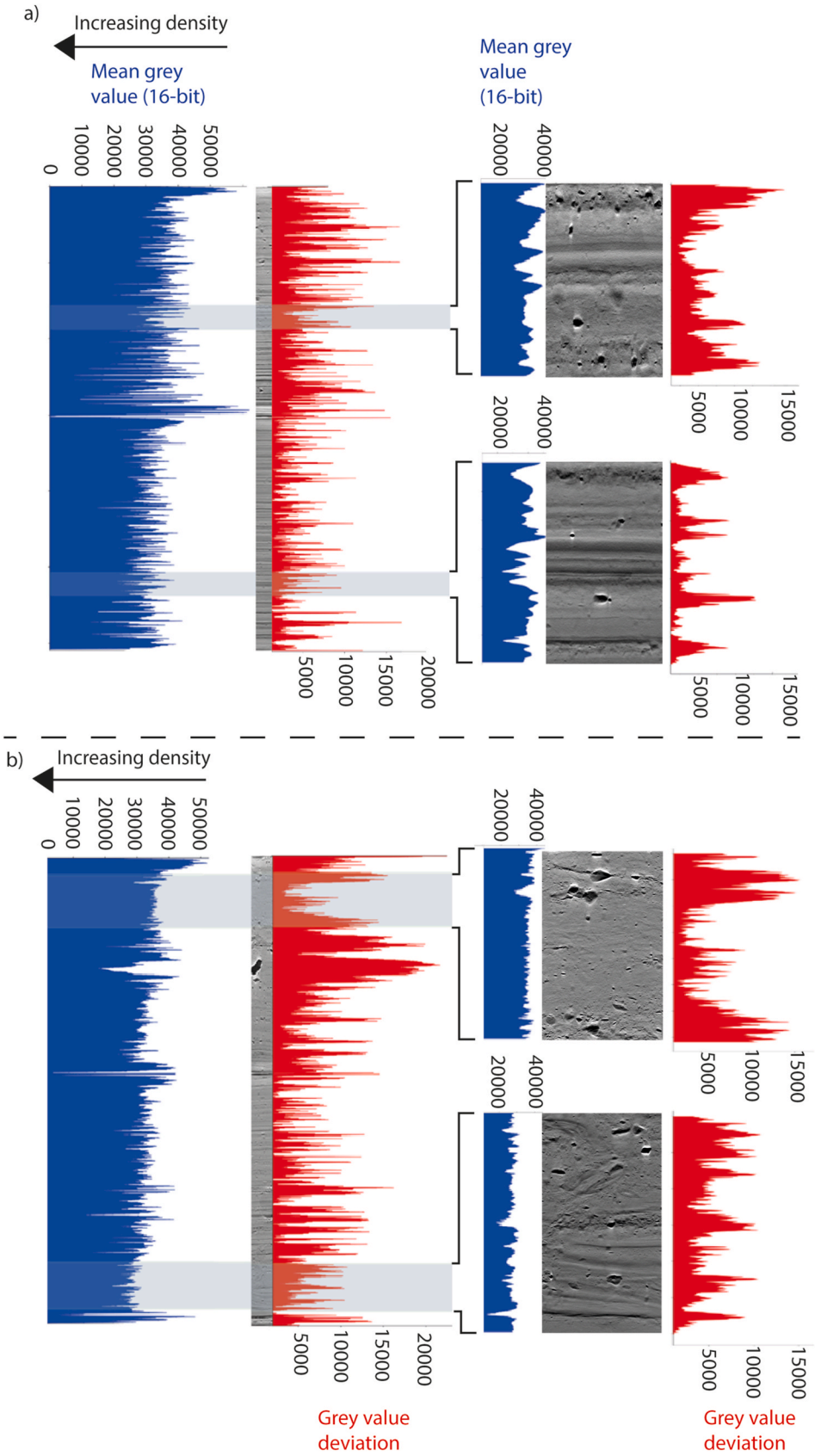

Fig. 6. Grey value mean and standard deviations at pixel-scale resolution (0.066 mm) downcore. a) Core sections JC123-032PC-section-05 and JC123-032PC-section-06. b) Core sections JC123-033PC-section-05 and JC123-033PC-section-06. Sub-section lengths approx. 10–20 cm.

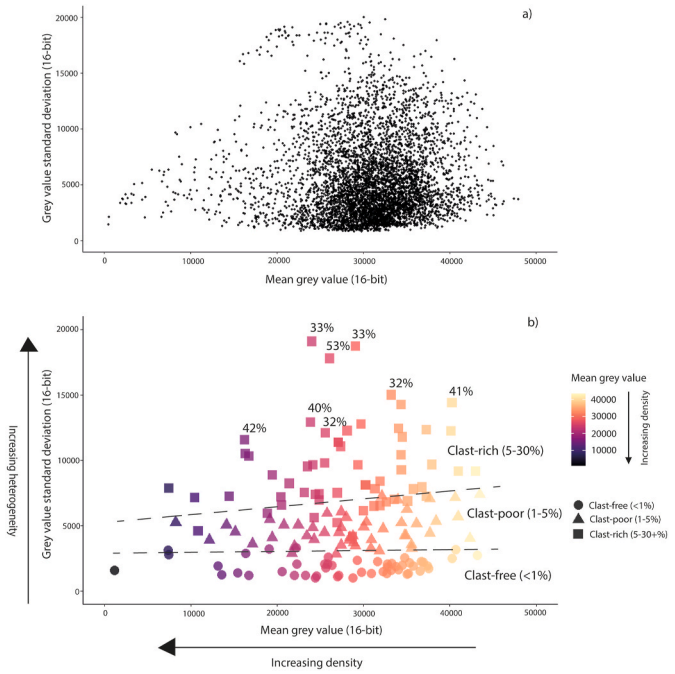

Fig. 7. a) Sediments in cores JC123-032PC-section05 + 06 and JC123-033PC-section-05 + 06 characterised by X-ray greyscale properties (mean grey value and standard deviation at pixel resolution). GV data systematically sampled at 10-pixel downcore intervals; b) Sediment classification by greyscale properties, dissected using modified Folk classification (Long, 2006). Colour of symbol indicates fine-grained sediment density. Shapes denote true % of clasts per Folk class. Each class contains a minimum of 50 data points, optically discriminated into dense (n = 25) and less dense sediments (n = 25) randomly sampled by mean grey value and associated standard deviation. (For interpretation of the references to colour in this figure legend, the reader is referred to the Web version of this article.)

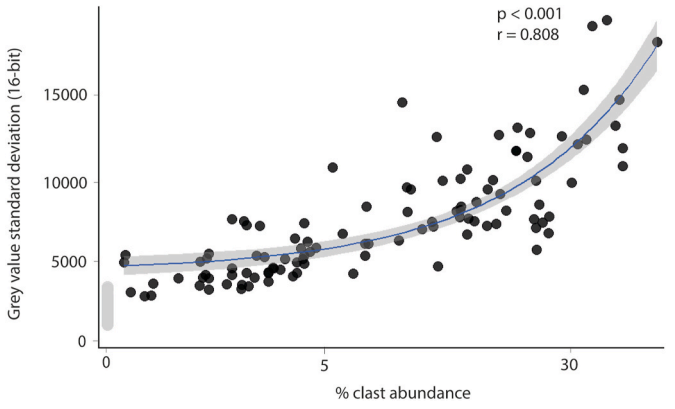

Fig. 8. Grey value deviation (16-bit) vs clast abundance (%) measured at pixel-scale resolution. Clast-free sediments (<1%) highlighted in grey near origin (excluded from correlation). Note: log scale on x-axis to aid data visualisation.

findings that a strong positive correlation exists between % area of clasts (>~0.5 mm) and the sum of GV SD per cm (Fig. 5). Although a degree of overlap was noted within facies (between % clast abundance and GV SD), our results suggest that the statistical difference between classes is sufficient to automatically quantify gravel abundance and therefore classify sediments based on the clastic component. Notably, outliers increase in abundance with increasing gravel (IRD) content (Fig. 8).

4.3. Inaccuracies associated with sediment heterogeneity as an IRD proxy

A few factors may account for the inaccuracies and outliers when predicting gravel abundance using sediment heterogeneity. Firstly, a lack of synchroneity in the magnitude is observed between all three IRD methods, this is probably due to the three distinctly different measurement techniques mentioned previously. The relationship between heterogeneity (GV SD) in glaciomarine sediments and clast abundance (%) (or IRD) is further complicated by several phenomena. Clasts may differ in composition giving unequal GV results between different rock types of identical size (or mass). Some clasts may also appear faint (unrepresentatively high GV, suggesting lower than true density) if they lie outside or are only partially within the CL region of interest (Fig. 10b) – similar partial volume effects have been noted by others to complicate the segmentation process (e.g. Withers et al., 2021). Such clasts were treated in the same way as all other clasts when creating 'clast maps' to maintain consistency but this may lead to underestimations in GV SD IRD measurements when compared to other IRD detection methods. An artifact which is more common in the CL images than XR and CT are bright 'halos'; these are associated with clasts with a high contrast between the clast-matrix media (Fig. 10a iv). These artifacts can lead to overestimations of matrix densities and clast abundance. However, as this effect is highly associated with clasts, correction is considered beyond the scope of this study. Additionally, the disadvantages of this scanning artifact in CL images are offset significantly when compared with XR, with a trade-off for increased image detail and a reduction in other artifacts e.g. beam hardening, cupping and striping. Investigations into reducing certain CL artifacts are currently ongoing (Bradley and Shreeve, 2020).

Non-clastic heterogeneous structures are found to be a common factor leading to overestimations in IRD. Occasionally, high GV SD occur due to measurements across laminae boundaries (Fig. 10a i). Such overestimations are characterised by GV SD pulses which are high in magnitude but short in distance (downcore); these can be picked out by sudden erratic peaks in area charts (Fig. 6). Matrix density variations are interpreted to result in the lower correlation coefficient in JC123-032PC-section-06 (r = 0.72) in comparison to other cores (e.g. the structureless matrix-supported diamicton JC123-033PC-section-05).

Similar GV SD overestimations are observed relating to other non-clastic heterogeneities. Examples include sediment with abundant flocculated laminae (Fig. 10a ii), wavy laminae or deformation structures (Fig. 10a iii), biogenics, bioturbation and mud pellets. These non-clastic heterogeneities may lead to overestimations in apparent IRD content (GV SD) and, if not recognised, could have implications when attempting to automatically quantify IRD content in different sediments. We therefore stress that this automated tool should be viewed and implemented as a measure of sediment heterogeneity, but that it can also be used as a proxy to infer IRD in sediment with a horizontally homogeneous sediment matrix. Combining sediment heterogeneity (GV SD) with on-screen grain counting may allow for a more accurate and comprehensive understanding of sediment structures and IRD, as different IRD measurement techniques can produce varying results (cf Andrews, 2000; Bartels et al., 2018).

There are a number of effects from piston core sampling which may potentially lead to inaccuracies in greyscale imaging properties. These sampling artifacts may include flow-in (Jutzeler et al., 2014) which can lead to data loss, or to the inclusion of poorly consolidated or highly fluidized sediment. Ultimately, any compression of sediment during sampling can lead to overestimations in sediment radiodensity (lower mean GV), with extensions of sedimentary structures resulting in underestimations (Skinner and McCave, 2003).

The maximum theoretical SD of a 16-bit greyscale image with a greyscale value range of 0–65535 ≈ 32767. The maximum SD would require 50% clast abundance to allow for sufficient deviation within the dataset (Fig. 11a). Thus, the relationship between GV SD and clast abundance (%) likely breaks down at clast abundances >50%, with

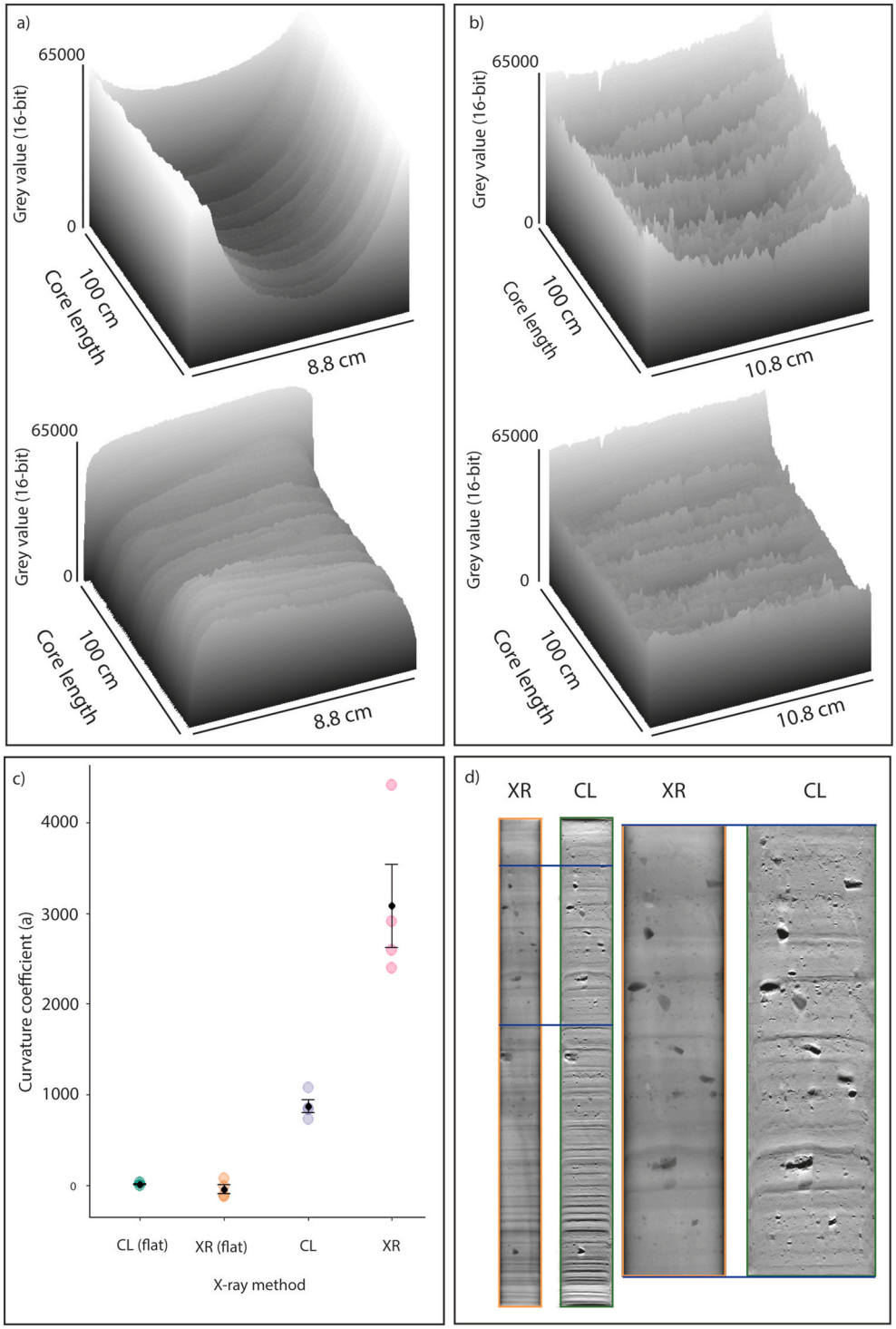

Fig. 9. Comparison of X-radiography (XR) and X-ray computed laminography (CL). a) and b) Surface plots of images for each scan (JC123-032PC-section-06) before (top) and after (bottom) beam hardening corrections (a = XR; b = CL). c) Comparison of curvature coefficients between scanning methods and image treatments (flat = post-beam hardening correction for each image). d) Side by side comparison of XR and CL images with glaciomarine sediments from core JC123-032PC-section-05. The lower detail observed in XR images is the result of excessive X-ray attenuation and lower geometric magnification (Zuber et al., 2017).

increasing uncertainty of GV SD at clast abundances >30% (Fig. 7b). Matrix sediment with higher GV can also lead to overestimations of clast abundance and vice versa (Fig. 11b). We deem this statistical phenomenon unavoidable, as the coefficient of variation was found to be a significantly weaker IRD proxy, with significant overestimations observed in dense matrix sediments. Despite these phenomena, a statistically significant relationship is observed between clast abundance (%) and GV SD ($p < 0.001$).

4.4. Sediment mean GV (radiodensity) as a proxy for energy of sediment deposition

Homogenous clast-free laminae can be indicative of a range of different glaciomarine environments (Ó Cofaigh and Dowdeswell, 2001; Maddison et al., 2005; Normandeau et al., 2017; Jennings et al., 2018; Smith et al., 2019), where the delivery of sediment-laden meltwater controls the character of glaciomarine sediment (Dowdeswell et al., 2001) with laminae density largely dependent on the energy of water flow at the time of deposition. The radiodensity of sediments could therefore be a powerful under-used proxy in deciphering the nature of

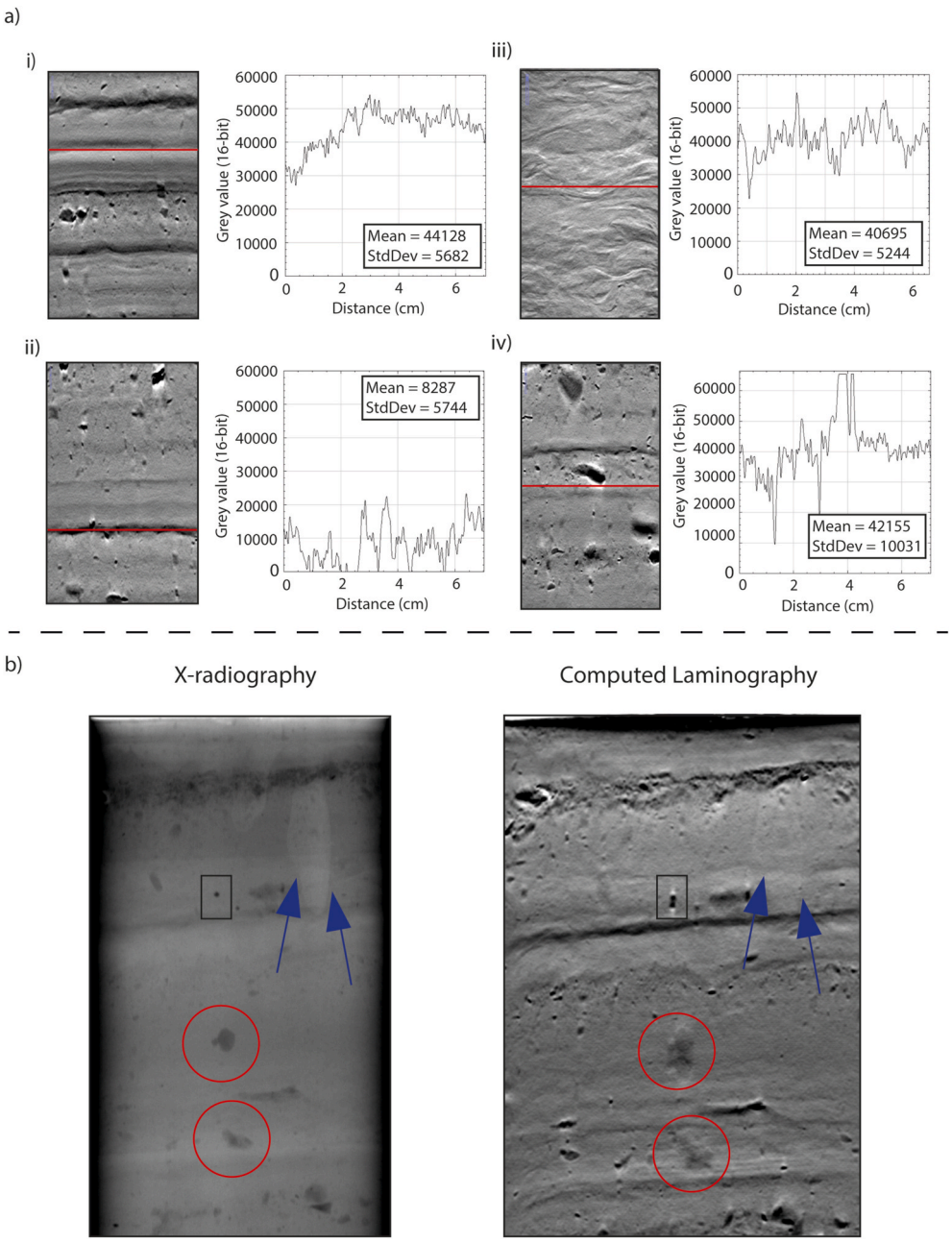

Fig. 10. a) Examples of overestimations in sediment characterisation from: i) laminae boundaries; ii) flocculated silts; iii) wavy laminae; iv) bright clast-edge 'halo'. b) Other examples of artifacts: 'ghost clasts' outwith scanning region of interest in CL (red circles); Bright halos at clast edges (black boxes); surface artifact reduced in CL image (blue arrows). (For interpretation of the references to colour in this figure legend, the reader is referred to the Web version of this article.)

deposition. As previously stated, for the cores in this study the fine sediment matrix appears to be the largest control on mean sediment radiodensity and the difference in laminae density is concurrent with changes in the mean grain size and composition of mud-silt couplets – with the finest-grained mud representing very low-energy settling and coarser silt indicating more energetic subaqueous deposition (Bradwell et al., 2021). This suggests that sediment radiodensity in fine-grained material could be indicative of the energy of deposition, in line with Vandorpe et al. (2019) who highlight a causal relationship between high X-ray attenuation coefficients (in Hounsfield units) and increased marine bottom-current activity. However, differing sediment provenance (e.g. alternating carbonate vs mafic mineral assemblages) resulting in differing radiodensities could also explain the variations in matrix GV between laminae. We suggest that higher radiodensity (lower mean GV) silt/mud glaciomarine sediments in this study are probably typical of minerogenic laminae of higher energy, probably terrigenous, origin (mean GV < 28000); conversely, lower radiodensity sediments (higher mean GV) are more typical of lower energy laminae of predominantly marine/biogenic origin (mean GV > 28000). Alternatively, in laminated sediments suspension settling could also be a factor, with coarse material settling first followed by finer material, giving rise to the cyclic variations in radiodensity. As the abundance (%) of clasts increases, the relative effect of matrix density on mean GV decreases. Therefore, to maintain the highest degree of predictive power, we suggest that the clast-free and clast-poor Folk classes provide the best proxy for sediment pathway and energy of deposition.

Despite the theoretically sound and robust relationships identified in this study, there are limitations with this approach. The density of glaciomarine sediments can be a function of phenomena other than transport energy or transport distance, as the relationship between bulk

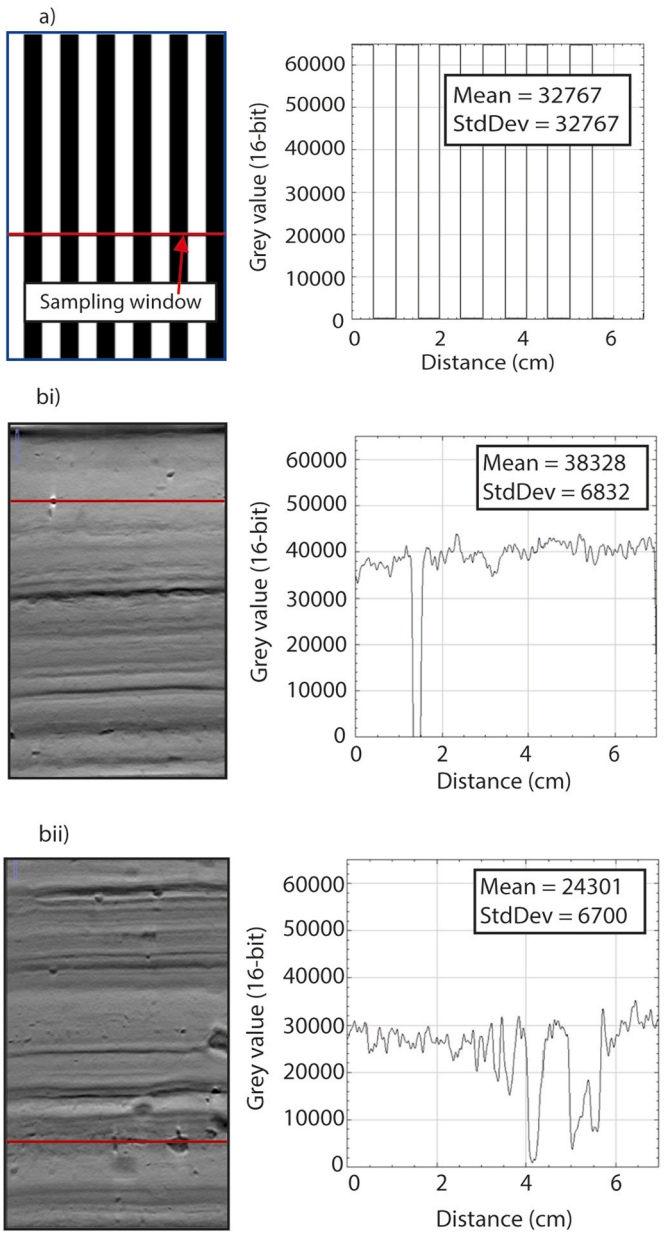

Fig. 11. Statistical phenomena associated with using GV SD as a proxy for % clast abundance (IRD): a) maximum GV SD of 16-bit GV image; bi) overestimations due to small dense clast in low density (high GV) matrix; bii) underestimations due to clasts of variable radiodensity embedded within dense matrix.

density and particle size/particle density is not a 1:1 relationship (McCave and Hall, 2006). Other factors affecting fine-sediment fraction density in glaciomarine settings include fine-sediment flocculation, sediment compaction (Crémer et al., 2002), and (partial) cementation (Hodell et al., 2017). The incorporation of rock flour or any other fine (silt-sized IRD) from icebergs and/or ice shelves/ice tongues to form dense silty fines may also be a factor in density overestimations (Hesse and Khodabakhsh, 2006). This problem has been observed in reconstructions of deep-sea bottom current velocities when using high-resolution particle-size analysis to discriminate sorted silts (bottom current material) from heterogeneous fines (IRD) (Jonkers et al., 2015). The increased resolution and detail of CL over CT helps to mitigate this effect.

5. Conclusions

The findings of this study show encouraging results for a new non-destructive, automated image-analysis technique of glaciomarine sediments. A number of significant findings are summarised:

1) Computed laminography (CL) images are better suited to quantitative analyses of cored glaciomarine sediments than traditional 2D X-radiography for two main reasons: (i) image quality is greatly increased, evidenced by an enhanced clarity of features (particularly clasts), higher contrast and sharper detail within the 'thin slice' plane of view; (ii) artifacts are found to be significantly reduced (beam hardening, striping and surface effects), although there is an increase in clast-edge 'halos'.
2) CL acquisition and processing produces smaller datasets compared to full 3D computed tomography (CT) but at significantly higher resolution than medical-grade CT imaging – resolving sedimentary structures and gravels which presently can only be identified using higher-resolution CT scanners made specifically for geological applications. As CL is cheaper, more efficient and less data intensive than CT, it offers multiple benefits, especially if absolute radiodensities (in Hounsfield Units) are not required.
3) Sediment heterogeneity measured by grey value standard deviation (GV SD) of CL imagery provides a very good approximation of clast abundance (%) in cored sediments with a strong statistically significant linear correlation ($r = 0.72–0.87$) ($p < 0.001$). GV SD can therefore be used as a proxy for IRD in glaciomarine sediments. Using our Sediment Characterisation tool (in the form of a FIJI/ImageJ plugin), IRD can be derived automatically at pixel-scale resolution. We hope this technique will improve efficiency but also improve resolution over existing IRD-identification methods.
4) Combining CL sediment heterogeneity (GV SD) with mean GV – a measure of sediment radiodensity – allows for automated classifications of marine and glaciomarine sediments into Folk sediment classes. This classification system could also be used to define the nature of sediment deposition in a range of marine settings.

In addition to the numerous benefits of this new technique, there are however certain drawbacks. Firstly, X-ray CL despite being better suited to GV quantification, suffers from certain artifacts which XR and CT are less affected by. These include: bright clast-edge 'halos' and out-of-plane features outwith the scanning region of interest. Sediment heterogeneity (GV SD) may also be better suited to quantifying clast abundances in certain sediments than others. A horizontally homogenous matrix (over the width of the core) is desirable, otherwise non-clastic variations in GV SD are also measured. These overestimations can be largely corrected for in regularly inclined laminated sediments by rotating images accordingly prior to analysis.

Finally, this study was borne out of the recent trend toward standardised practices using automated open-access tools for analysing glaciomarine sediment. We hope that the application of CL in Quaternary science will enable new tools and new practices to be implemented to rapidly and non-destructively characterise high-value glaciomarine sediments. Additionally, we propose that the tools presented in this study should have broader applications in the geosciences beyond glaciomarine sediment classification and IRD quantification including: precise varve counting; the identification of bioturbation structures; void space quantification (porosity); and sediment deformation analyses.

Declaration of competing interest

The authors declare that they have no known competing financial interests or personal relationships that could have appeared to influence the work reported in this paper.

Acknowledgements

Collection of the marine cores used in this work was funded by the UK Natural Environment Research Council consortium grant BRITICE-CHRONO NE/J009768/1. We thank the BGS Marine Operations team and NOC/NMFSS coring team for their help during JC123. We also thank the master and crew of the RRS *James Cook* (JC123). This work was funded by the Natural Environment Research Council as part of an IAPETUS2 Doctoral Training Partnership (N. McDonald).

Appendix A. Supplementary data

Supplementary data to this article can be found online at https://doi.org/10.1016/j.qsa.2021.100046.

References

Andrews, J.T., 2000. Icebergs and iceberg rafted detritus (IRD) in the North Atlantic: facts and assumptions. Oceanography 13 (3), 100–108. https://doi.org/10.5670/oceanog.2000.19.

Andresen, C.S., Straneo, F., Ribergaard, M.H., 2011. Rapid response of Helheim Glacier in Greenland to climate variability over the past century. Nat. Geosci. 5, 37–41. https://doi.org/10.1038/ngeo1349.

Bartels, M., Titschack, J., Fahl, K., Stein, R., Seidenkrantz, M.-S., Hillaire-Marcel, C., Hebbeln, D., 2017. Atlantic Water advection vs. glacier dynamics in northern Spitsbergen since early deglaciation. Clim. Past 13, 1717–1749. https://doi.org/10.5194/cp-13-1717-2017.

Bartels, M., Titschack, J., Fahl, K., Stein, R., Hebbeln, D., 2018. Wahlenbergfjord, eastern Svalbard: a glacier-surrounded fjord reflecting regional hydrographic variability during the Holocene? Boreas 47, 1003–1021. https://doi.org/10.1111/bor.12325.

Bradley, R.S., Shreeve, J., 2020. 'Bringing laminography to the realms of geoscience'. [PowerPoint presentation]. iRIS-2020 international rock imaging summit. Available online athttps://www.researchgate.net/publication/348566292. . (Accessed 9 August 2021).

Bradwell, T., Fabel, D., Clark, C.D., Chiverrell, R.C., Small, D., Smedley, R.K., Saher, M. H., Moreton, S.G., Dove, D., Callard, S.L., Duller, G.A.T., Medialdea, A., Bateman, M. D., Burke, M.J., McDonald, N., Gilgannon, S., Morgan, S., Roberts, D.H., Ó Cofaigh, C., 2021. Pattern, style and timing of British–Irish Ice Sheet advance and retreat over the last 45000years :evidence from NW Scotland and the adjacent continental shelf. J. Quat. Sci. 36 (5), 871–933. https://doi.org/10.1002/jqs.3296.

Bond, G.C., Lotti, R., 1995. Iceberg discharges into the North-Atlantic on millennial time scales during the last glaciation. Science 267 (5200), 1005–1010. https://doi.org/10.1126/science.267.5200.1005.

Clark, C.D., Hughes, A.L.C., Greenwood, S.L., Jordan, C., Sejrup, H.P., 2012. Pattern and timing of retreat of the last British–Irish Ice Sheet. Quat. Sci. Rev. 44, 112–146. https://doi.org/10.1016/j.quascirev.2010.07.019.

Condron, A., Hill, J.C., 2021. Timing of iceberg scours and massive ice-rafting events in the subtropical North Atlantic. Nat. Commun. 12, 3668. https://doi.org/10.1038/s41467-021-23924-0.

Crémer, J.-F., Long, B., Desrosiers, G., de Montety, L., Locat, J., 2002. Application de la scanographie à l'étude de la densité des sédiments et à la caractérisation des structures sédimentaires: exemple des sédiments déposés dans la rivière Saguenay (Québec, Canada) après la crue de juillet. Can. Geotech. J. 39 (2), 440–450. https://doi.org/10.1139/t01-101.

Damci, E., Çağatay, M.N., 2015. An automated algorithm for dating annually laminated sediments using X-ray radiographic images, with applications to Lake Van (Turkey), Lake Nautajarvi (Finland) and Byfjorden (Sweden). Quat. Int. https://doi.org/10.1016/j.quaint.2015.05.007.

Dowdeswell, J.A., Whittington, R.J., Jennings, A.E., Andrews, J.T., Mackensen, A., Marienfeld, P., 2000. An origin for laminated glacimarine sediments through sea-ice build-up and suppressed iceberg rafting. Sedimentology 47, 557–576. https://doi.org/10.1046/j.1365-3091.2000.00306.x.

Dowdeswell, J.A., Ó Cofaigh, C., Andrews, J.T., Scourse, J.D., 2001. Workshop explores debris transported by icebergs and paleoenvironmental implications. Eos Trans. AGU 82 (35), 382–386. https://doi.org/10.1029/01EO00239.

Favier, L., Durand, G., Cornford, S., Gudmundsson, G.H., Gagliardini, O., Gillet-Chaulet, F., Payne, A., Le Brocq, A.M., 2014. Retreat of Pine Island Glacier controlled by marine ice-sheet instability. Nat. Clim. Change 4, 117–121. https://doi.org/10.1038/nclimate2094.

Fisher, H.D., Jørgensen, J.S., Gajjar, P., Behnsen, J., Lionheart, W.R., Withers, P.J., 2019. Laminography in the lab: imaging planar objects using a conventional x-ray CT scanner. Meas. Sci. Technol. 30 (12), 035401 https://doi.org/10.1088/1361-6501/aafcae.

Francus, P., Kanamaru, K., Fortin, D., 2015. Standardization and calibration of X-radiographs acquired with the ITRAX core scanner. In: Croudace, I., Rothwell, R. (Eds.), Micro-XRF Studies of Sediment Cores. Developments in Paleoenvironmental Research, 17. Springer, Dordrecht. https://doi.org/10.1007/978-94-017-9849-5_20.

Gowan, E.J., Zhang, X., Khosravi, S., Rovere, A., Stocchi, P., Hughes, A.L.C., Gyllencreutz, R., Mangerud, Svendsen, J.-I., Lohmann, G., 2021. A new global ice sheet reconstruction for the past 80000years. Nat. Commun. *12*, 1199. https://doi.org/10.1038/s41467-021-21469-w.

Grobe, H., 1987. A simple method for the determination of ice-rafted debris in sediment cores. Polarforschung 57 (3), 123–126 https://doi.org/10013/epic.11658.d001.

Graham, A., Kuhn, G., Meisel, O., Hillenbrand, C.-D., Hodgson, D., Hermann, W., Wacker, L., Winterstaller, P., Dos Santos Ferriera, C., Römer, M., White, D., Bohrmann, G., 2017. Major advance of South Georgia glaciers during the Antarctic Cold Reversal following extensive sub-Antarctic glaciation. Nat. Commun. 8, 4798. https://doi.org/10.1038/ncomms14798.

Gondrom, S., Zhou, J., Maisl, M., Reiter, H., Kröning, M., Arnold, W., 1999. X-ray computed laminography: an approach of computed tomography for applications with limited access. Nucl. Eng. Des. 190 (1–2), 141–147. https://doi.org/10.1016/S0029-5493(98)00319-7.

Heinrich, H., 1988. Origin and consequences of cyclic ice rafting in the northeast Atlantic Ocean during the past 130,000 years. Quat. Res. 29, 142–152. https://doi.org/10.1016/0033-5894(88)90057-9.

Helfen, L., Myagotin, A., Rack, A., Pernot, P., Mikulík, P., Di Michiel, M., Baumbach, T., 2007. Synchrotron-radiation computed laminography for high-resolution three-dimensional imaging of flat devices. Physics status solidi (a) 204 (8), 2760–2765. https://doi.org/10.1002/pssa.200775676.

Hesse, R., Khodabakhsh, S., 2006. Significance of fine-grained sediment lofting from melt-water generated turbidity currents for the timing of glaciomarine sediment transport into the deep sea. Sediment. Geol. 186, 1–11. https://doi.org/10.1016/j.sedgeo.2005.10.006.

Hibbert, F.D., Austin, W.E.N., Leng, M.J., Gatliff, R.W., 2010. British Ice Sheet dynamics inferred from North Atlantic ice-rafted debris records spanning the last 175000years. J. Quat. Sci. 25, 461–482. https://doi.org/10.1002/jqs.1331.

Hodell, D.A., Nicholl, J.A., Bontognali, T.R.R., Danino, S., Dorador, J., Dowdeswell, J.A., Einsle, J., Kuhlmann, H., Martrat, B., Mleneck-Vautravers, M.J., Rodríguez-Tovar, F. J., Röhl, U., 2017. Anatomy of Heinrich Layer 1 and its role in the last deglaciation. Paleoceanography 32, 284–303. https://doi.org/10.1002/2016PA003028.

Jennings, A.E., Andrews, J.T., Ó Cofaigh, C., St-Onge, G., Belt, S., Cabedo-Sanz, P., Pearce, C., Hillaire-Marcel, C., Calvin Campbell, D., 2018. Baffin Bay paleoenvironments in the LGM and HS1: resolving the ice-shelf question. Mar. Geol. 402, 5–16. https://doi.org/10.1016/j.margeo.2017.09.002.

Joe, Y.J., Polyak, L., Schreck, M., Niessen, F., Yoon, S.H., Kong, G.S., Nam, S.I., 2020. Late quaternary depositional and glacial history of the arliss plateau off the east siberian margin in the western arctic ocean. Quat. Sci. Rev. 228, 106099 https://doi.org/10.1016/j.quascirev.2019.106099.

Jonkers, L., Barker, S., Hall, I.R., Prins, M.A., 2015. Correcting for the influence of ice-rafted detritus on grain size-based paleocurrent speed estimates. Paleoceanography 30, 1347–1357. https://10.1002/2015PA002830.

Jutzeler, M., White, J., Talling, P., Mccanta, M., Morgan, S., Le Fraint, A., Ishizuka, O., 2014. Coring disturbances in IODP piston cores with implications for offshore record of volcanic events and the Missoula megafloods. Geochem. Geophys. Geosys AGU Geochem. Society 15 (9), 3572–3590. https://doi.org/10.1002/2014GC005447.

Kilfeather, A., Ó Cofaigh, C., Lloyd, J., Dowdeswell, J., Xu, S., Moreton, S., 2011. Ice-stream retreat and ice-shelf history in marguerite trough, Antarctic Peninsula: sedimentological and foraminiferal signatures. GSA Bulletin 123 (5-6), 997–1015. https://doi.org/10.1130/B30282.1.

Long, D., 2006. BGS detailed explanation of seabed sediment modified folk classification. MESH report. British Geol. Surv.

Maddison, E.J., Pike, J., Leventer, A., Domack, E.W., 2005. Deglacial seasonal and sub-seasonal diatom record from Palmer Deep, Antarctica. J. Quat. Sci. 20, 435–446. https://doi.org/10.1002/jqs.947.

Margari, V., Skinner, L.C., Menviel, L., Capron, E., Rhodes, R.H., Mleneck-Vautravers, M. J., Ezat, M.M., Martrat, B., Grimalt, J.O., Hodell, D.A., Tzedakis, P.C., 2020. Fast and slow components of interstadial warming in the North Atlantic during the last glacial. Commun. Earth Environ. 1, 6. https://doi.org/10.1038/s43247-020-0006-x.

McCave, I., Hall, I., 2006. Size sorting in marine muds: processes, pitfalls, and prospects for paleoflow-speed proxies. G-cubed 71 (10). https://doi.org/10.1029/2006GC001284.

Mena, A., Francés, G., Pérez-Arlucea, M., Aguiar, P., Barreiro-Vázquez, J.-D., Iglesias, A., Barreiro, A., 2015. A novel sedimentological method based on CT-scanning: use for tomographic characterization of the Galicia Interior Basin. Sediment. Geol. 321, 123–138. https://doi.org/10.1016/j.sedgeo.2015.03.007.

Normandeau, A., Lajeunesse, P., Trottier, A.-P., Poiré, A., Pienitz, R., 2017. Sedimentation in isolated glaciomarine embayments during glacio-isostatically induced relative sea level fall (northern Champlain Sea basin). Can. J. Earth Sci. 54 (10), 1049–1062. https://doi.org/10.1139/cjes-2017-0002.

Ó Cofaigh, C., Dowdeswell, J.A., 2001. Laminated sediments in glacimarine environments: diagnostic criteria for their interpretation. Quat. Sci. Rev. 20 (13), 1411–1436. https://doi.org/10.1016/S0277-3791(00)00177-3.

Obrochta, S.P., Crowley, T.J., Channell, J.E.T., Hodell, D.A., Baker, P.A., Seki, A., Yokoyama, Y., 2014. Climate variability and ice-sheet dynamics during the last three glaciations. Earth Planet Sci. Lett. 406, 198–212. https://doi.org/10.1016/j.epsl.2014.09.004.

O'Regan, M., Cronin, T., rly, B., Alstrup, A.K.O., Gemery, L., Golub, A., Mayer, L.A., Morlighem, M., Moros, M., Munk, O.L., Nilsson, J., Pearce, C., Detlef, H., Stranne, C., Vermassen, F., West, G., Jakobsson, M., 2021. The Holocene dynamics of Ryder Glacier and ice tongue in north Greenland. Cryosphere 15, 4073–4097. https://doi.org/10.5194/tc-2021-95.

Pierce, E.L., van de Flierdt, T., Williams, T., Hemming, S.R., Cook, C.P., Passchier, S., 2017. Evidence for a dynamic East Antarctic ice sheet during the mid-Miocene climate transition. Earth Planet Sci. Lett. 478, 1–13. https://doi.org/10.1016/j.epsl.2017.08.011.

Principato, S., 2005. X-ray radiographs of sediment cores: a guide to analyzing diamicton. In: Francus, P. (Ed.), Image Analysis, Sediments and Paleoenvironments.

Developments in Paleoenvironmental Research, 7. Springer, Dordrecht. https://doi.org/10.1007/1-4020-2122-4_9.
Reilly, B.T., Stoner, J.S., Wiest, J., 2017. SedCT: MATLAB™ tools for standardized and quantitative processing of sediment core computed tomography (CT) data collected using a medical CT scanner. G-cubed 18, 3231–3240. https://10.1002/2017GC006884.
Reilly, B.T., Stoner, J.S., Mix, A.C., Walczak, M.H., Jennings, A., Jakobsson, M., Dyke, L., Glueder, A., Nicholls, K., Hogan, K.A., Mayer, L.A., Hatfield, R.G., Albert, S., Marcott, S., Fallon, S., Cheseby, M., 2019. Holocene break-up and reestablishment of the Petermann ice tongue, Northwest Greenland. Quat. Sci. Rev. 218, 322–342. https://doi.org/10.1016/j.quascirev.2019.06.023.
Rignot, E., Casassa, G., Gogineni, P., Krabill, W., Rivera, A., Thomas, R., 2004. Accelerated ice discharge from the Antarctic Peninsula following the collapse of Larsen B ice shelf. Geophys. Res. Lett. 31, L18401. https://doi.org/10.1029/2004GL020697.
Scambos, T.A., Bohlander, J.A., Shuman, C.A., Skvarca, P., 2004. Glacier acceleration and thinning after ice shelf collapse in the Larsen B embayment, Antarctica. Geophys. Res. Lett. 31, L18402. https://doi.org/10.1029/2004GL020670.
Schoof, C., 2007. Ice sheet grounding line dynamics: steady states, stability, and hysteresis. J. Geophys. Res. 112, F03S28. https://doi.org/10.1029/2006JF000664.
Schindelin, J., Arganda-Carreras, I., Frise, E., Kaynig, V., Longair, M., Pietzsch, T., Preibisch, S., Rueben, C., Saalfeld, S., Schmid, B., Tinevez, J.-Y., White, D.J., Hartenstein, V., Eliceiri, K., Tomancak, P., Cardona, A., 2012. Fiji: an open-source platform for biological-image analysis. Nat. Methods 9 (7), 676–682. https://doi.org/10.1038/nmeth.2019.
Scourse, J., Haapaniemi, A., Colmenero-Hidalgo, E., Peck, V., Hall, I., Austin, W., Knutz, P., Zahn, R., 2009. Growth, dynamics and deglaciation of the last British-Irish ice sheet: the deep-sea ice-rafted detritus record. Quat. Sci. Rev. 28, 3066–3084. https://doi.org/10.1016/j.quascirev.2009.08.009.
Skinner, L.C., McCave, I., 2003. Analysis and modeling of gravity- and piston coring based on soil mechanics. Mar. Geol. 199, 181–204. https://doi.org/10.1016/S0025-3227(03)00127-0.
Smith, J.A., Graham, A.G.C., Post, A.L., Hilenbrand, C.-D., Bart, P.J., Powell, R.D., 2019. The marine geological imprint of Antarctic ice shelves. Nat. Commun. 10, 5635. https://doi.org/10.1038/s41467-019-13496-5.
Starr, A., Hall, I.R., Barker, S., Rackow, T., Zhang, Xu, Hemming, S.R., van der Lubbe, H.J.L., Knorr, G., Berke, M.A., Bigg, G.R., Cartagena-Sierra, A., Jiménez-Espejo, F.J., Gong, X., Gruetzner, J., Nambiyathodi, L., LeVay, L.J., Robinson, R.S., Ziegler, M., Expedition 361 Science Party, 2021. Antarctic icebergs reorganize ocean circulation during Pleistocene glacials. Nature 589, 236–241. https://doi.org/10.1038/s41586-020-03094-7.
St-Onge, G., Long, B.F., 2009. CAT-scan analysis of sedimentary sequences: an ultrahigh-resolution paleoclimatic tool. Eng. Geol. 103 (3–4), 127–133. https://doi.org/10.1016/j.enggeo.2008.06.016.
Syvitski, J.P.M., Andrews, J.T., Dowdeswell, J.A., 1996. Sediment deposition in an iceberg-dominated glacimarine environment, East Greenland: basin fill implications. Global Planet. Change 12, 251–270. https://doi.org/10.1016/0921-8181(95)00023-2.
Tonai, S., Kubo, Y., Tsang, M., 2019. A new method for quality control of geological cores by X-ray computed tomography: application in IODP expedition 370. Front. Earth Sci. 7, 1–13. https://doi.org/10.3389/feart.2019.00117.
Vandorpe, T., Collart, T., Cnudde, V., Lebreiro, S., Hernández-Molina, F.J., Alonso, B., Mena, A., Antón, L., Van Rooij, D., 2019. Quantitative characterisation of contourite deposits using medical CT. Mar. Geol. 417, 106003. https://doi.org/10.1016/j.margeo.2019.106003.
Vermassen, F., Wangner, D.J., Dyke, L.M., Schmidt, S., Cordua, A.E., Kjær, K.H., Haubner, K., Andresen, C.S., 2019. Evaluating ice-rafted debris as a proxy for glacier calving in Upernavik Isfjord, NW Greenland. J. Quat. Sci. 34, 258–267. https://doi.org/10.1002/jqs.3095.
Vermassen, F., Bjørk, A.A., Sicre, M.-A., Jaeger, J.M., Wangner, D.J., Kjeldsen, K.K., Siggaard-Andersen, M.-L., Klein, V., Mouginho, J., Kjær, K.H., Andresen, C.A., 2020. A major collapse of Kangerlussuaq Glacier's ice tongue between 1932 and 1933 in East Greenland. Geophys. Res. Lett. 47 https://doi.org/10.1029/2019GL085954 e2019GL085954.
Withers, P.J., Bouman, C., Carmignato, Cnudde, V., Grimaldi, D., Hagen, C.K., Maire, E., Manley, M., Du Plessis, A., Stock, S.R., 2021. X-ray computed tomography. Nat. Rev. Methods Primers 1, 18. https://doi.org/10.1038/s43586-021-00015-4.
Xu, F., Helfen, L., Baumbach, T., Suhonen, H., 2012. Comparison of image quality in computed laminography and tomography. Opt Express 20, 794–806. https://doi.org/10.1364/OE.20.000794.
Zuber, M., Laaß, M., Hamann, E., Kretschmer, S., Hauschke, N., van de Kamp, T., Baumbach, T., Koenig, T., 2017. Augmented laminography, a correlative 3D imaging method for revealing the inner structure of compressed fossils. Sci. Rep. 7, 41413. https://doi.org/10.1038/srep41413.